PHOTONICS Research

Room temperature III–V nanolasers with distributed Bragg reflectors epitaxially grown on (001) silicon-on-insulators

Yu Han,[1,†] Wai Kit Ng,[2,†] Ying Xue,[1] Kam Sing Wong,[2,3] and Kei May Lau[1,4]

[1]Department of Electronic and Computer Engineering, Hong Kong University of Science and Technology, Clear Water Bay, Kowloon, Hong Kong, China
[2]Department of Physics and William Mong Institute of Nano Science and Technology, Hong Kong University of Science and Technology, Clear Water Bay, Kowloon, Hong Kong, China
[3]e-mail: phkwong@ust.hk
[4]e-mail: eekmlau@ust.hk

Received 31 May 2019; revised 13 July 2019; accepted 30 July 2019; posted 30 July 2019 (Doc. ID 368995); published 27 August 2019

Efficient, scalable, bufferless, and compact III–V lasers directly grown on (001)-oriented silicon-on-insulators (SOIs) are preferred light sources in Si-photonics. In this article, we present the design and operation of III–V telecom nanolaser arrays with integrated distributed Bragg reflectors (DBRs) epitaxially grown on industry-standard (001) SOI wafers. We simulated the mirror reflectance of different guided modes under various mirror architectures, and accordingly devised nanoscale DBR gratings to support high reflectivity around 1500 nm for the doughnut-shaped TE_{01} mode. Building from InP/InGaAs nanoridges grown on SOI, we fabricated subwavelength DBR mirrors at both ends of the nanoridge laser cavities and thus demonstrated room-temperature low-threshold InP/InGaAs nanolasers with a 0.28 μm^2 cross-section and a 20 μm effective cavity length. The direct growth of these bufferless nanoscale III–V light emitters on Si-photonics standard (001) SOI wafers opens future options of fully integrated Si-based nanophotonic integrated circuits in the telecom wavelength regime.

https://doi.org/10.1364/PRJ.7.001081

1. INTRODUCTION

Epitaxial growth of III–V light emitters on (001)-oriented Si substrates provides an intriguing alternative to the bonding approach for the realization of fully integrated Si-photonics chips [1,2]. Such a monolithic integration scheme is compatible with the currently scalable, high-yield, and cost-effective manufacturing process offered by electronics foundries. Recent studies highlight the demonstration of room-temperature operation, low threshold, and high reliability III–V laser diodes directly grown on Si wafers using quantum dots as the active gain medium and engineered III–V/Si templates for minimal dislocation densities [3–5]. Using various defect trapping and filtering techniques, the defect density of current III–V/Si templates has been reduced to the order of 10^6 cm^{-2} for GaAs on Si and 10^8 cm^{-2} for InP on Si, respectively [6–8]. However, the several micron thick III–V buffer needed for defect reduction makes it difficult for the integration of the III–V light sources with the Si waveguides underneath. While present research focuses on high-performance individual laser diodes grown on Si substrates, future applications require efficient on-chip coupling of III–V lasers with Si-based photonic and electronic devices, and therefore necessitate bufferless III–V light emitters directly grown on (001)-oriented SOI wafers [9].

Bufferless III–V nanostructures with various compositions and architectures have been selectively grown on patterned (001) Si and SOI substrates [10–18], and subsequently enabled optically pumped nanoridge lasers with different emission wavelengths [19–22]. Despite the subwavelength scale of the cross-section of these nanolasers, the length of the nanocavities, however, is usually longer than 50 μm to compensate for cavity loss and sustain room temperature laser oscillation. This issue aggravates at longer wavelengths, particularly in the strategically important telecom bands, due to the increasing intrinsic and mirror losses [23]. A cavity length of 100 μm is required to support room-temperature O-band lasing inside suspended InP/InGaAs nanocavities on bulk Si substrates [20]. The continuing miniaturization of the laser footprint improves the integration density and reduces the power dissipation of Si-based photonic integrated circuits [24–26]. Scaling down the device dimension also opens new applications beyond optical interconnects and data processing, such as sensing, medical imaging, holography, and many more [27,28]. In contrast to

the conventional Fabry–Perot (FP) cavity, creation of ultrasmall laser sources usually relies on advanced cavity designs with minimum mirror loss. Examples include microdisk lasers [29], photonic crystal cavity lasers [30,31], and lasers with integrated gratings/mirrors, such as vertical-cavity surface-emitting lasers (VCSELs) [32].

In our earlier work, we demonstrated room-temperature InP/InGaAs nanolasers selectively grown on (001) SOI wafers [33]. These inplane nanolasers feature FP cavities with optical feedback provided by reflections from the InP/air interface. Owing to the inefficient optical feedback, cavity length longer than 50 μm is required to support lasing in the S- and C-band. Aiming at minimizing the footprint of the nanolasers, in this paper, we incorporate distributed Bragg reflectors (DBRs) at the ends of the 1500 nm band nanocavity lasers, and demonstrate InP/InGaAs nanolasers with subwavelength DBRs epitaxially grown on (001) SOI wafers. The nanoscale DBRs significantly reduce the cavity loss, and consequently scale the length of the nanolasers down to approximately 20 μm and enable room-temperature low-threshold stable lasing operation at the S-band. We design the laser structures by theoretically studying the reflectivity and mirror loss of the subwavelength DBRs and then experimentally confirm our design through fabrication of nanolasers with integrated DBRs. The design and room-temperature operation of these tiny coherent light emitters on (001) SOI wafers point to future integration with Si-based nanoscale optoelectronic circuits.

2. DESIGN OF NANOSCALE DBRS

Figure 1(a) depicts the architecture of the designed nanolasers with integrated DBRs on SOI substrates. Two sets of DBRs, consisting of periodically arranged InP spacers and air gaps, provide optical feedback for laser oscillation, and the sandwiched InP/InGaAs nanoridge serves as the gain medium for optical amplification. Unlike FP lasers with a large portion of light coupled out from the cavity, the periodic structures of DBRs allow for close-to-unit reflections and thereby produce high-quality optical resonators [Fig. 1(b)]. Figure 1(c) delineates the cross-sectional structure of the designed nanolasers. The air-cladded InP/InGaAs nanoridge stands atop the buried oxide layer with an intermediate Si pedestal for mechanical support. The designed nanolaser builds on the inplane, millimeter-long InP/InGaAs nanoridges directly grown on patterned (001) SOI wafers [34,35], as shown by the scanning electron microscope (SEM) image in Fig. 1(d). Five InGaAs ridge quantum wells embedded inside the InP nanoridge function as the active gain medium. Figure 1(e) displays the transmission electron microscopy (TEM) image of one as-grown InP/InGaAs nanoridge. Selective area growth inside {111}-enclosed Si trenches eliminates the formation of antiphase boundaries, confines the generated crystalline defects at the III–V/Si interface, and thereby circumvents the use of thick III–V buffers for effective defect reduction [36]. The proposed nanolaser structure can be completed via removal of the SiO_2 spacers with buffered oxide etch and undercutting the Si device layer with KOH-based anisotropic wet etching. This is followed by focused ion beam (FIB) milling to define the nanoscale DBR gratings through the InP/InGaAs nanoridges at the ends

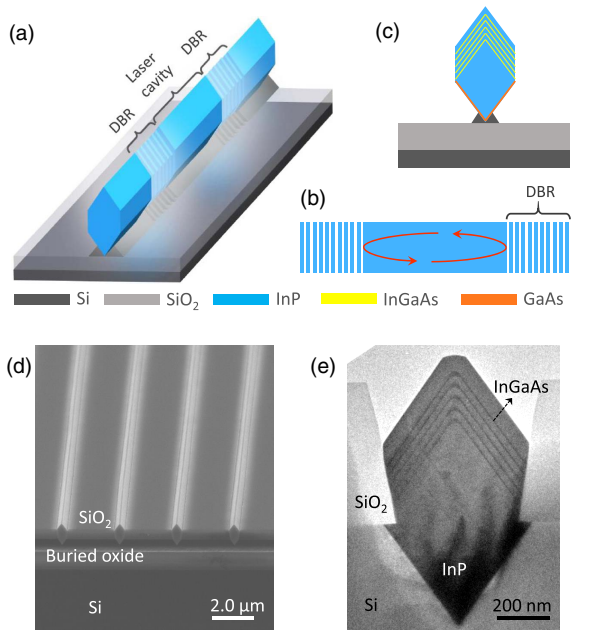

Fig. 1. (a) Schematic of the InP/InGaAs nanolaser with DBRs directly grown on (001)-oriented SOI wafers. The nanocavity and the two DBRs are marked. (b) Schematic depicting the improved optical feedback from the two defined DBRs. (c) Cross-sectional schematic of the InP/InGaAs nanolaser on SOI. Five $In_{0.53}Ga_{0.47}As$ ridge quantum wells are embedded as the active gain medium. (d) Tilted-view SEM photo of the as-grown InP/InGaAs nanoridges on (001) SOI wafers. (e) Cross-sectional TEM image of the as-grown InP/InGaAs nanoridge on SOI wafers.

of the nanolaser cavities. An oxide protection layer was deposited atop the nanoridges before the Ga-based ion milling process and was subsequently removed after the grating fabrication. A low probe current of 1.2 nA at 30 kV was chosen to minimize the redeposition effects.

The subwavelength characteristic of the InP/InGaAs nanoridges suggests a different light-matter interaction mechanism from the conventional thin-film-based macroscopic lasers. We adopted two-dimensional finite-difference-eigenmode and three-dimensional finite-difference-time-domain simulations to study the guided transverse modes and corresponding mirror reflectivity under different mirror configurations. Figure 2(b) displays the simulated mode profiles of the first three guided modes, namely HE_{11a}, HE_{11b}, and TE_{01}. The identification of the modes guided in the air-cladded nanoridges follows the principle of cylindrical dielectric waveguides [37]. Figure 2(a) summarizes the calculated mirror reflectance from the InP/air interface and the designed 2nd-order DBR gratings with different parameters. We chose the 2nd-order grating instead of the 1st-order grating for the ease of device fabrication. The DBRs are designed to ensure a maximum mirror reflectivity of around 1500 nm, which is also the photoluminescence (PL) emission peak of the as-grown InP/InGaAs nanoridges. Without DBRs, the tightly confined HE_{11a} mode features a mirror reflectivity of 33% at 1500 nm, a similar value to macroscopic laser bars with cleaved end facets. Interestingly, the HE_{11b} mode has a higher mirror reflectivity of 51%, and the less-confined TE_{01} mode

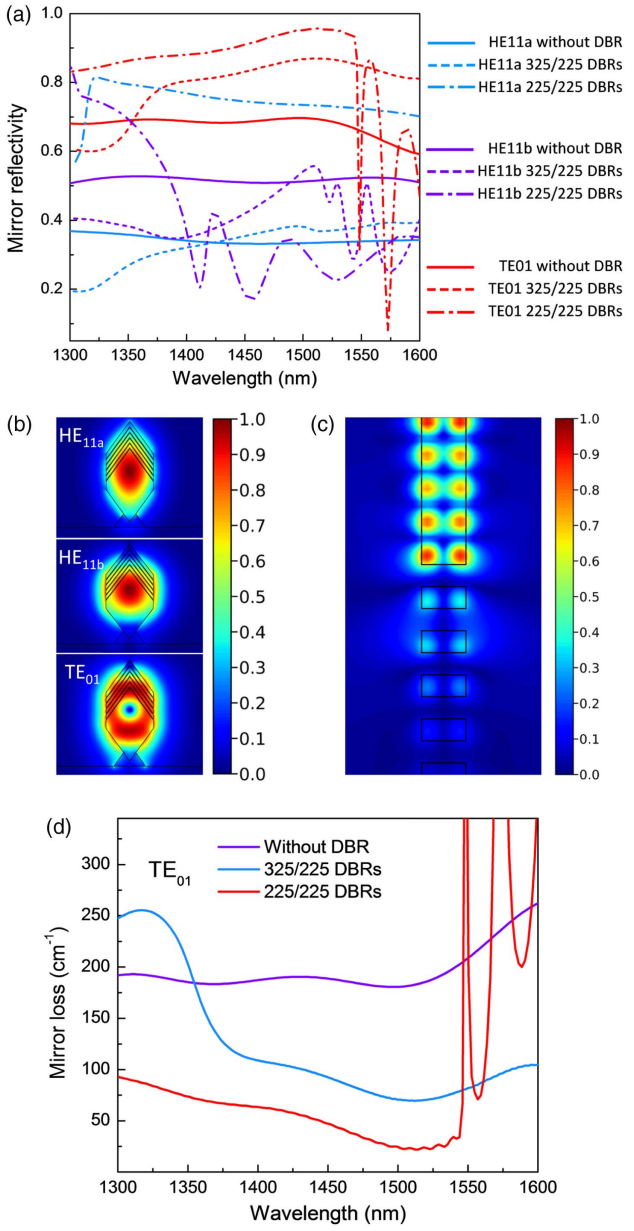

Fig. 2. Design of nanoscale DBRs with different parameters. (a) Calculated reflectivity from InP/air interface, 10 periods of DBRs with 325 nm InP and 225 nm air gaps, and 10 periods of DBRs with 225 nm InP and 225 nm air gaps. (b) Mode profiles of the first three supported transverse modes. (c) Calculated electric field distribution of the TE_{01} mode with the introduction of 10 periods of DBRs with 225 nm InP and 225 nm air gaps. (d) Calculated mirror loss of the TE_{01} mode of a 20 μm long nanocavity with different mirror architectures.

exhibits the highest mirror reflectivity of 70% at 1500 nm. The spectra of mirror reflectance change drastically when introducing 10 periods of DBRs. Under DBRs with 325 nm InP spacers and 225 nm air gaps, the reflectivity of both the HE_{11a} and the HE_{11b} modes at 1500 nm increases slightly, while the value of the TE_{01} mode improves to over 87%. When tailoring the InP spacers to 225 nm and maintaining the same air gaps, the reflectivity of the TE_{01} mode at 1500 nm increases progressively to 95%. The reflectivity of the HE_{11a} and the HE_{11b} modes, however, changes to 74% and 30%, respectively. The sharp dips in the reflection spectra indicate the photonic band edge of the DBR gratings. Figure 2(c) depicts the electric filed distribution of the TE_{01} mode at the interface of the DBRs (225 nm InP spacers and air gaps) and the nanoridge waveguide, exemplifying the enhanced mirror reflectance brought by the designed DBRs. As a result, the TE_{01} mode experiences the highest optical feedback and is most likely to lase under all three configurations. This claim is further underpinned by the fact that the TE_{01} mode manifests the largest overlap with active gain medium, benefiting from the doughnut-shaped mode profile and the ridge nature of the InGaAs quantum wells [see Fig. 2(b)]. At 1500 nm the quantum well confinement factors of the HE_{11a} mode, the HE_{11b} mode, and the TE_{01} mode are 5.66%, 5.29%, and 6.48%, respectively. Note that we designed the gratings to support high reflectivity for the TE_{01} mode, which exhibits the largest overlap with the active region and thereby could enable the shortest laser cavity. By carefully tuning the grating parameters, it is possible to shift the peak reflectivity of the fundamental mode to the 1500 nm band and enable lasing from the fundamental mode, which is more favorable in actual optical communications.

A 25% increase of the mirror reflectivity might seem insignificant. However, the improvement becomes apparent when translating the values into mirror losses. We calculated the roundtrip mirror loss using the equation of $\alpha_m = -\frac{1}{L}\ln \tilde{R}$, where L refers to the length of the nanocavity and $\tilde{R}$ represents the geometric mean of the mirror reflectivity. Since a 20 μm long nanolaser without any DBRs cannot sustain room temperature stimulated emission, we thus set L at 20 μm to demonstrate the efficacy of the designed DBRs. Figure 2(d) presents the calculated loss of the TE_{01} mode with different mirror architectures. The mirror loss reduces significantly from 181 cm^{-1} without any DBRs to 71 cm^{-1} and then to 23 cm^{-1} with the introduction of nanoscale DBRs. Note that because of the large refractive index contrast between the InP spacers and the air gaps, the designed DBRs feature a broad spectra and might support multimode lasing behavior. In contrast, distributed feedback (DFB) gratings could enable single-mode lasing and precise wavelength control. However, DFB lasers entail a much larger number of grating periods to obtain sufficient mirror reflectivity and consequently have a much longer cavity length, usually larger than 100 μm to support lasing in the telecom bands [19,38].

3. ROOM TEMPERATURE NANOLASERS ON SOI

Figures 3(a) and 3(b) display the top-view and tilted-view SEM photos of the fabricated InP/InGaAs nanolasers with integrated DBRs on SOI substrates. Each nanolaser comprises a 20 μm long active waveguide section and two sets of DBR mirrors. The DBR mirror consists of 10 periods of alternating InP spacers and air gaps, as shown in the zoomed-in SEM photos imaged from different angles in Figs. 3(c) and 3(d). The InP spacers have a slight taper from the bottom Si pedestal to the top nanoridge tip [see the closeup SEM photo in Fig. 4(e)]. Based on our calculations, we fabricated three sets of devices, including 20 μm long FP nanolasers without any DBRs,

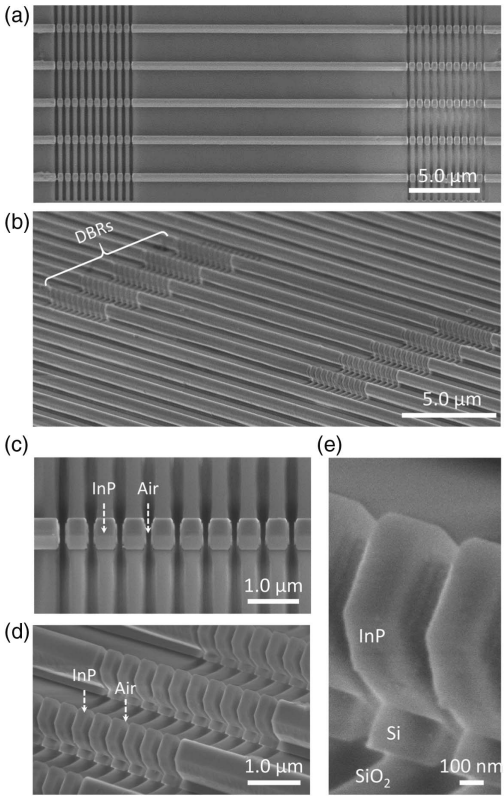

Fig. 3. (a) Top view SEM image of the fabricated InP/InGaAs nanolasers with defined DBRs (325 nm InP spacers and 225 nm air gaps) on SOI. (b) Tilted-view SEM image of InP/InGaAs nanolasers with labeled DBRs. (c) Zoomed-in SEM photo of one DBR composed of InP spacers and air gaps. (d) Zoomed-in SEM photo of one DBR showing the etched InP spacers and air gaps. (e) Close-up showing the details of the DBRs. The InP spacer exhibits a tapered morphology from the bottom to the top.

nanolasers with DBRs consisting of 325 nm InP spacers and 225 nm air gaps, and nanolasers with DBRs consisting of 225 nm InP spacers and 225 nm air gaps.

We characterized the fabricated nanolasers on SOI using a home-built micro-PL system. A mode-locked Ti/sapphire laser (750 nm, 100 fs pulse width, and 76 MHz repetition rate) delivers optical excitation, and a thermoelectric-cooled InGaAs detector collects light emission from the probed nanolasers. As only a tiny part of the laser emission is collected and analyzed, an arbitrary unit is adopted in all the PL measurements. Figure 4(a) shows the room temperature emission spectra of one 20 μm long nanolaser without any DBRs. Equally spaced FP resonance peaks appear under low excitation, however, fail to evolve into lasing peaks when excitation increases to higher levels due to uncompensated mirror loss. Figure 4(b) displays the room-temperature emission spectra of one nanolaser with integrated DBRs (325 nm InP spacers and 225 nm air gaps). Similarly, resonance modes emerge under low excitation levels. Benefiting from the reduced mirror loss, one mode at 1442 nm transforms into a lasing peak and stands out from the noisy spontaneous background as excitation ramps up to 48.1 μJ/cm^2. Figure 4(c) presents the room-temperature emission spectra of one nanolaser with another set of DBRs (225 nm InP spacers and 225 nm air gaps). As a result of the ultra-low cavity loss, strong lasing occurs at a longer wavelength of 1478 nm under a lower pumping level of only 38.4 μJ/cm^2. Two adjacent side modes also arise above the threshold and strengthen alongside the dominant lasing peak, which stems from the synergy of the broad reflection spectra of the DBRs and the wide gain spectra of the InGaAs ridge quantum wells. The side-mode suppression ratios (SMSRs) are 7.5 dB and 6.3 dB for nanolasers with 352/225 DBRs and 225/225 DBRs, respectively.

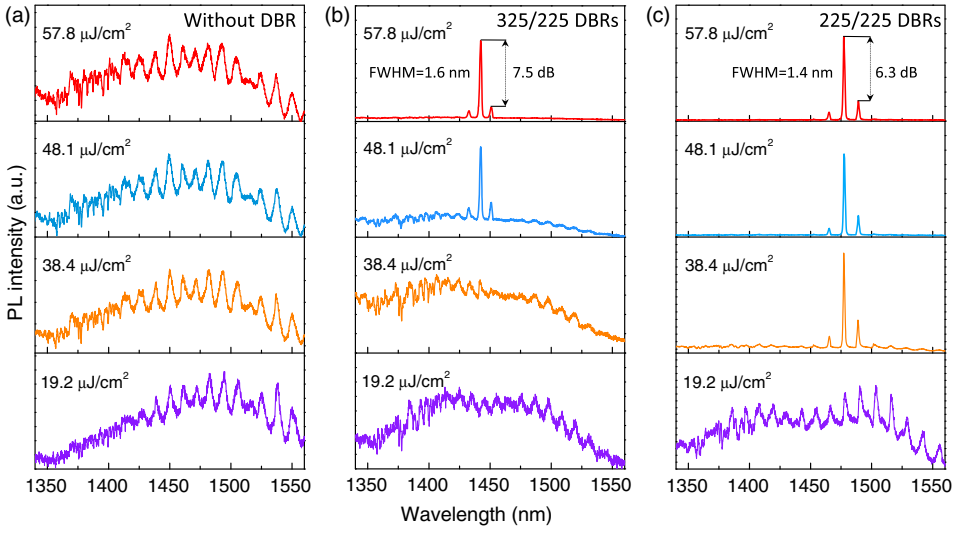

Fig. 4. (a) Room temperature PL spectra of one InP/InGaAs nanolaser with conventional 20 μm long FP cavity under different excitation levels. Equally spaced FP modes are detected. (b) Room temperature PL spectra of one InP/InGaAs nanolaser with DBRs (325 nm thick InP spacers and 225 nm thick air gaps) and a 20 μm active waveguide section under different excitation levels. Stimulated emission at 1442 nm is detected. (c) Room temperature PL spectra of one InP/InGaAs nanolaser with DBRs (225 nm thick InP spacers and 225 nm thick air gaps) and a 20 μm active waveguide section under different excitation levels. Stimulated emission at 1478 nm is detected.

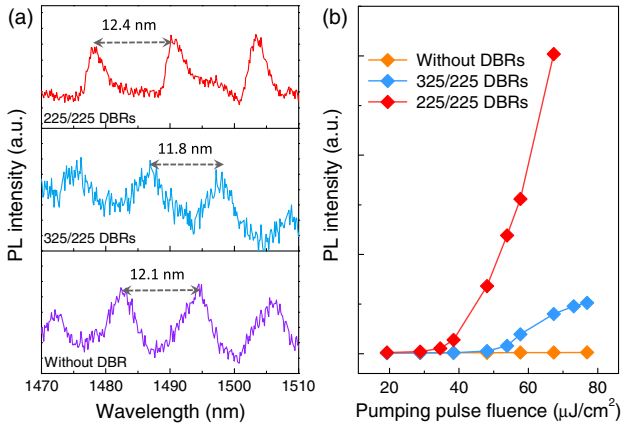

Fig. 5. (a) Zoomed-in emission spectra of three different InP/InGaAs nanolasers under low excitation levels. The free spectral ranges are marked. (b) Light in–light out (L-L) curves of the three measured InP/InGaAs nanolasers with/without DBRs.

Figure 5(a) compares the zoomed-in PL spectra around 1500 nm of the three probed nanolasers under low pumping levels. Inspection of the resonance modes reveals a free spectral range of around 12 nm and accordingly suggests a group refractive index of $n_g = 4.6$, based on the equation $\Delta\lambda = \frac{\lambda^2}{2Ln_g}$, where $\Delta\lambda$, λ, and L are the free spectral range, the emission wavelength, and the length of the nanocavity, respectively. This value agrees well with the $n_g = 4.4$ of TE_{01} obtained from the simulations, whereas HE_{11a} and HE_{11b} show a smaller group refractive index of 3.7 and 4.1 at around 1500 nm, respectively. The agreement between theory and experiment further corroborates that TE_{01} is the dominant mode in all the examined devices. Figure 5(b) plots the evolution of peak intensity as a function of the excitation levels (L-L curve). In contrast to the linear trend of nanolasers without any DBRs, devices with integrated DBRs exhibit a clear kink around the threshold, an unambiguous sign of strong lasing behavior and an evident proof for the efficacy of the defined DBRs. A threshold of 48 $\mu J/cm^2$ and 38 $\mu J/cm^2$ is extracted from the L-L curves for the two different sets of nanolasers with DBRs, respectively. The average pumping power delivered by the objective is selected for the calibration of the threshold values. Other considerations such as percentage of excitation light absorbed by the nanoridges or reflections from the SOI substrate are not estimated in our calculation. We ascribe the larger threshold of devices with 325 nm InP spacers to the larger mirror loss. In addition, it also requires a higher pumping level to reach population inversion at shorter wavelengths.

4. SUMMARY

In summary, we have presented the design and room temperature operation of telecom III–V nanolasers with integrated DBRs epitaxially grown on (001) SOI substrates. With extensive analysis of the mode reflectivity, we devised subwavelength DBRs that support high mirror reflectance around 1500 nm for the TE_{01} mode. The improved mirror design subsequently scales the length of the nanolasers down to 20 μm and enables low-threshold lasing operation at the S-band. Our demonstration here suggests an interesting path for the continuing miniaturization of III–V nanolasers and paves the way toward compact photonic integrated circuits processed on Si-photonics standard (001) SOI wafers. Building on the results here, future work includes single-mode operation of the on-chip nanolasers using advanced mode selection schemes. Electrically driven nanolasers on SOI can be realized by doping and making metal contacts to the III–V nanoridges. Incorporation of the nanolasers into Si photonic integrated circuits via coupling the nanolasers with Si waveguides can also be considered.

Funding. Research Grants Council, University Grants Committee (16212115, 16245216, AoE/P02/12); Innovation and Technology Fund (ITS/273/16FP); William Mong Institute of Nano Science and Technology (WMINST19/SC04).

Acknowledgment. The authors would like to thank the MCPF and NFF of HKUST for technical support. Helpful discussions with Sang Soon Oh, Qiang Li, and C. W. Tang are also acknowledged.

†These authors contributed equally to this work.

REFERENCES

1. D. Liang and J. E. Bowers, "Recent progress in lasers on silicon," Nat. Photonics **4**, 511–517 (2010).
2. Z. C. Wang, A. Abbasi, U. Dave, A. D. Groote, S. Kumari, B. Kunert, C. Merckling, M. Pantouvaki, Y. Shi, B. Tian, and K. Van Gasse, "Novel light source integration approaches for silicon photonics," Laser Photon. Rev. **11**, 1700063 (2017).
3. S. Chen, W. Li, J. Wu, Q. Jiang, M. Tang, S. Shutts, S. N. Elliott, A. Sobiesierski, A. J. Seeds, I. Ross, P. M. Smowton, and H. Liu, "Electrically pumped continuous-wave III-V quantum dot lasers on silicon," Nat. Photonics **10**, 307–311 (2016).
4. A. Y. Liu, C. Zhang, J. Norman, A. Snyder, D. Lubyshev, J. M. Fastenau, A. Liu, A. C. Gossard, and J. E. Bowers, "High performance continuous wave 1.3 μm quantum dot lasers on silicon," Appl. Phys. Lett. **104**, 041104 (2014).
5. Y. Wan, J. Norman, Q. Li, M. J. Kennedy, D. Liang, C. Zhang, D. Huang, Z. Zhang, A. Y. Liu, A. Torres, D. Jung, A. C. Gossard, E. L. Hu, K. M. Lau, and J. E. Bowers, "1.3 μm submilliamp threshold quantum dot micro-lasers on Si," Optica **4**, 940–944 (2017).
6. D. Jung, R. Herrick, J. Norman, K. Turnlund, C. Jan, K. Feng, A. C. Gossard, and J. E. Bowers, "Impact of threading dislocation density on the lifetime of InAs quantum dot lasers on Si," Appl. Phys. Lett. **112**, 153507 (2018).
7. B. Kunert, Y. Mols, M. Baryshniskova, N. Waldron, A. Schulze, and R. Langer, "How to control defect formation in monolithic III/V heteroepitaxy on (100) Si? A critical review on current approaches," Semicond. Sci. Technol. **33**, 093002 (2018).
8. Q. Li and K. M. Lau, "Epitaxial growth of highly mismatched III-V materials on (001) silicon for electronics and optoelectronics," Prog. Cryst. Growth Charact. Mater. **63**, 105–120 (2017).
9. D. Thomson, A. Zilkie, J. E. Bowers, T. Komljenovic, G. T. Reed, L. Vivien, D. Marris-Morini, E. Cassan, L. Virot, J. M. Fédéli, and J. M. Hartmann, "Roadmap on silicon photonics," J. Opt. **18**, 073003 (2016).
10. J. Z. Li, J. Bai, J.-S. Park, B. Adekore, K. Fox, M. Carroll, A. Lochtefeld, and Z. Shellenbarger, "Defect reduction of GaAs epitaxy on Si (001) using selective aspect ratio trapping," Appl. Phys. Lett. **91**, 021114 (2007).
11. C. Merckling, N. Waldron, S. Jiang, W. Guo, N. Collaert, M. Caymax, E. Vancoille, K. Barla, A. Thean, M. Heyns, and W. Vandervorst, "Heteroepitaxy of InP on Si (001) by selective-area metal organic

vapor-phase epitaxy in sub-50 nm width trenches: the role of the nucleation layer and the recess engineering," J. Appl. Phys. **115**, 023710 (2014).
12. T. Orzali, A. Vert, B. O'Brian, J. L. Herman, S. Vivekanand, S. S. Rao, and S. R. Oktyabrsky, "Epitaxial growth of GaSb and InAs fins on 300 mm Si (001) by aspect ratio trapping," J. Appl. Phys. **120**, 085308 (2016).
13. B. Kunert, W. Guo, Y. Mols, B. Tian, Z. Wang, Y. Shi, D. Van Thourhout, M. Pantouvaki, J. Van Campenhout, R. Langer, and K. Barla, "III/V nano ridge structures for optical applications on patterned 300 mm silicon substrate," Appl. Phys. Lett. **109**, 091101 (2016).
14. Y. Han, Q. Li, and K. M. Lau, "Highly ordered horizontal indium gallium arsenide/indium phosphide multi-quantum-well in wire structure on (001) silicon substrates," J. Appl. Phys. **120**, 245701 (2016).
15. W. Guo, L. Date, V. Pena, X. Bao, C. Merckling, N. Waldron, N. Collaert, M. Caymax, E. Sanchez, E. Vancoille, and K. Barla, "Selective metal-organic chemical vapor deposition growth of high quality GaAs on Si (001)," Appl. Phys. Lett. **105**, 062101 (2014).
16. L. Megalini, B. Bonef, B. C. Cabinian, H. Zhao, A. Taylor, J. S. Speck, J. E. Bowers, and J. Klamkin, "1550-nm InGaAsP multi-quantum-well structures selectively grown on v-groove-patterned SOI substrates," Appl. Phys. Lett. **111**, 032105 (2017).
17. S. Li, X. Zhou, M. Li, X. Kong, J. Mi, M. Wang, W. Wang, and J. Pan, "Ridge InGaAs/InP multi-quantum-well selective growth in nanoscale trenches on Si (001) substrate," Appl. Phys. Lett. **108**, 021902 (2016).
18. Y. Han, Y. Xue, and K. M. Lau, "Selective lateral epitaxy of dislocation-free InP on silicon-on-insulator," Appl. Phys. Lett. **114**, 192105 (2019).
19. Z. C. Wang, B. Tian, M. Pantouvaki, W. Guo, P. Absil, J. V. Campenhout, C. Merckling, and D. V. Thourhout, "Room-temperature InP distributed feedback laser array directly grown on silicon," Nat. Photonics **9**, 837–842 (2015).
20. Y. Han, Q. Li, S. Zhu, K. W. Ng, and K. M. Lau, "Continuous-wave lasing from InP/InGaAs nanoridges at telecommunication wavelengths," Appl. Phys. Lett. **111**, 212101 (2017).
21. B. Tian, Z. Wang, M. Pantouvaki, P. Absil, J. V. Campenhout, C. Merckling, and D. V. Thourhout, "Room temperature O-band DFB laser array directly grown on (001) silicon," Nano Lett. **17**, 559–564 (2016).
22. Y. Shi, Z. Wang, J. V. Campenhout, M. Pantouvaki, W. Guo, B. Kunert, and D. V. Thourhout, "Optical pumped InGaAs/GaAs nano-ridge laser epitaxially grown on a standard 300 mm Si wafer," Optica **4**, 1468–1473 (2017).
23. Y. Ma, X. Guo, X. Wu, L. Dai, and L. Tong, "Semiconductor nanowire lasers," Adv. Opt. Photon. **5**, 216–273 (2013).
24. F. Lu, I. Bhattacharya, H. Sun, T. D. Tran, K. W. Ng, G. N. Malheiros-Silveira, and C. C. Hasnain, "Nanopillar quantum well lasers directly grown on silicon and emitting at silicon-transparent wavelengths," Optica **4**, 717–723 (2017).
25. Y. Han, W. K. Ng, C. Ma, Q. Li, S. Zhu, C. C. S. Chan, K. W. Ng, S. Lennon, R. A. Taylor, K. S. Wong, and K. M. Lau, "Room-temperature InP/InGaAs nano-ridge lasers grown on Si and emitting at telecom bands," Optica **5**, 918–923 (2018).
26. G. Zhang, M. Takiguchi, K. Tateno, T. Tawara, M. Notomi, and H. Gotoh, "Telecom-band lasing in single InP/InAs heterostructure nanowires at room temperature," Sci. Adv. **5**, eaat8896 (2019).
27. R. Ma and R. F. Oulton, "Applications of nanolasers," Nat. Nanotechnol **14**, 12–22 (2019).
28. M. T. Hill and M. C. Gather, "Advances in small lasers," Nat. Photonics **8**, 908–918 (2014).
29. S. L. McCall, A. F. J. Levi, R. E. Slusher, S. J. Pearton, and R. A. Logan, "Whispering-gallery mode microdisk lasers," Appl. Phys. Lett. **60**, 289–291 (1992).
30. H. Park, S. Kim, S. Kwon, Y. Ju, J. Yang, J. Baek, S. Kim, and Y. Lee, "Electrically driven single-cell photonic crystal laser," Science **305**, 1444–1447 (2004).
31. H. Kim, W. Lee, A. C. Farrell, A. Balgarkashi, and D. L. Huffaker, "Telecom-wavelength bottom-up nanobeam lasers on silicon-on-insulator," Nano Lett. **17**, 5244–5250 (2017).
32. J. L. Jewell, J. P. Harbison, A. Scherer, Y. Lee, and L. T. Florez, "Vertical-cavity surface-emitting lasers: design, growth, fabrication, characterization," IEEE J. Quantum Electron. **27**, 1332–1346 (1991).
33. Y. Han, W. K. Ng, Y. Xue, Q. Li, K. S. Wong, and K. M. Lau, "Telecom InP/InGaAs nanolaser array directly grown on (001) silicon-on-insulator," Opt. Lett. **44**, 767–770 (2019).
34. Y. Han, Q. Li, S. Chang, W. Hsu, and K. M. Lau, "Growing InGaAs quasi-quantum wires inside semi-rhombic shaped planar InP nanowires on exact (001) silicon," Appl. Phys. Lett. **108**, 242105 (2016).
35. Y. Han, Q. Li, K. W. Ng, S. Zhu, and K. M. Lau, "InGaAs/InP quantum wires grown on silicon with adjustable emission wavelength at telecom bands," Nanotechnology **29**, 225601 (2018).
36. M. Paladugu, C. Merckling, R. Loo, O. Richard, H. Bender, J. Dekoster, W. Vandervorst, M. Caymax, and M. Heyns, "Site selective integration of III-V materials on Si for nanoscale logic and photonic devices," Cryst. Growth Des. **12**, 4696–4702 (2012).
37. E. Snitzer, "Cylindrical dielectric waveguide modes," J. Opt. Soc. Am. **51**, 491–498 (1961).
38. Y. Wang, S. Chen, Y. Yu, L. Zhou, L. Liu, C. Yang, M. Liao, M. Tang, Z. Liu, J. Wu, and W. Li, "Monolithic quantum-dot distributed feedback laser array on silicon," Optica **5**, 528–533 (2018).